ULTRAFAST DYNAMICS

Attosecond band-gap dynamics in silicon

Martin Schultze,[1,2*†] Krupa Ramasesha,[1*] C.D. Pemmaraju,[3] S.A. Sato,[4] D. Whitmore,[1] A. Gandman,[1] James S. Prell,[1] L. J. Borja,[1] D. Prendergast,[3] K. Yabana,[4,5] Daniel M. Neumark,[1,6†] Stephen R. Leone[1,6,7†]

Electron transfer from valence to conduction band states in semiconductors is the basis of modern electronics. Here, attosecond extreme ultraviolet (XUV) spectroscopy is used to resolve this process in silicon in real time. Electrons injected into the conduction band by few-cycle laser pulses alter the silicon XUV absorption spectrum in sharp steps synchronized with the laser electric field oscillations. The observed ~450-attosecond step rise time provides an upper limit for the carrier-induced band-gap reduction and the electron-electron scattering time in the conduction band. This electronic response is separated from the subsequent band-gap modifications due to lattice motion, which occurs on a time scale of 60 ± 10 femtoseconds, characteristic of the fastest optical phonon. Quantum dynamical simulations interpret the carrier injection step as light-field–induced electron tunneling.

Excitation of electrons from valence band (VB) states into mobile conduction band (CB) states by light is one of the most fundamental phenomena in semiconductor physics. The dynamics of these charge carriers have been extensively studied previously on multifemtosecond to microsecond time scales, providing insight into postexcitation processes such as carrier cooling, transport, and electron-hole recombination (*1*). However, the buildup and interaction of carriers in the conduction band during excitation have thus far proven too rapid to probe directly. Interest in the time evolution of the excitation process is motivated by far-reaching implications regarding the ultimate speed of electronics (*2*), solid-state coherent control (*3*, *4*), and the mechanisms of dielectric breakdown (*5*–*7*). In previous experiments, only at very low excitation densities (*8*) or for quantum mechanically suppressed electron-phonon coupling has it been possible to disentangle electronic and lattice dynamics (*9*). Thus, a key question remained open as to whether the reduction of the measured band gap of semiconductors as a function of CB population [for optically (*10*)/thermally (*11*) excited or doped (*12*) samples] involves the rearrangement of the crystal lattice or is mainly a result of carrier-carrier interactions in the CB.

[1]Department of Chemistry, University of California, Berkeley, CA 94720, USA. [2]Fakultät für Physik, Ludwig-Maximilians-Universität, Am Coulombwall 1, D-85748 Garching, Germany. [3]The Molecular Foundry, Lawrence Berkeley National Laboratory, Berkeley, CA 94720, USA. [4]Graduate School of Pure and Applied Sciences, University of Tsukuba, Tsukuba 305-8571, Japan. [5]Center for Computational Sciences, University of Tsukuba, Tsukuba 305-8577, Japan. [6]Chemical Sciences Division, Lawrence Berkeley National Laboratory, Berkeley, CA 94720, USA. [7]Department of Physics, University of California, Berkeley, CA 94720, USA.
*These authors contributed equally to this work. **†Corresponding author. E-mail: martin.schultze@mpq.mpg.de (M.S.); dneumark@berkeley.edu (D.M.N.); srl@berkeley.edu (S.R.L.)**

Attosecond solid-state spectroscopy (*13*) in tandem with time-dependent density functional theory (TD-DFT) is used here to follow the initial steps of the excitation mechanism in real time in silicon. Probing the sample with isolated attosecond pulses near the silicon 2*p* core transition ($L_{2,3}$-edge at 99 eV) reveals that electrons excited across the band gap cause an instantaneous reduction of the band-gap energy due to carrier-carrier interactions evolving on an ~450-attosecond time scale. The electronic response is completed before the lattice motion affects the band gap, with a longer time constant of 60 ± 10 fs resembling the period of the fastest optical phonon in silicon of 64 fs (15.6 THz) (*14*, *15*).

The principles of attosecond transient absorption spectroscopy of semiconductors are illustrated in Fig. 1. The band structure of crystalline silicon accommodates both direct and indirect excitations of electrons across the band gap (Fig. 1A). At low intensities, a near-infrared (NIR) pump pulse can in principle promote electrons from the VB maximum across the indirect band gap (E_{gap} = 1.2 eV), satisfying momentum conservation by the addition of a phonon. However, at higher intensities above 10^{10} W/cm^2, the creation of electron hole pairs across the larger direct band gap (E_{gap} = 3.2 eV) becomes possible and dominates the transition rate. This transition occurs without phonon participation, but the larger energy separation of the direct band gap requires the simultaneous absorption of two or more NIR or visible photons (E_{photon} = 1.1 – 2.7 eV). Here, we establish that for light intensities of >10^{12} W/cm^2, electron tunneling driven by the electric field of light is the main excitation pathway.

Attosecond pulses tuned to the silicon $L_{2,3}$ edge centered at 99 eV, as displayed in Fig. 1A, are used to measure the dynamics of electrons injected into the CB by few-cycle NIR laser pump pulses. The probe pulses are shorter than 100 attoseconds, as confirmed by photoelectron streaking spectroscopy [see the supplementary

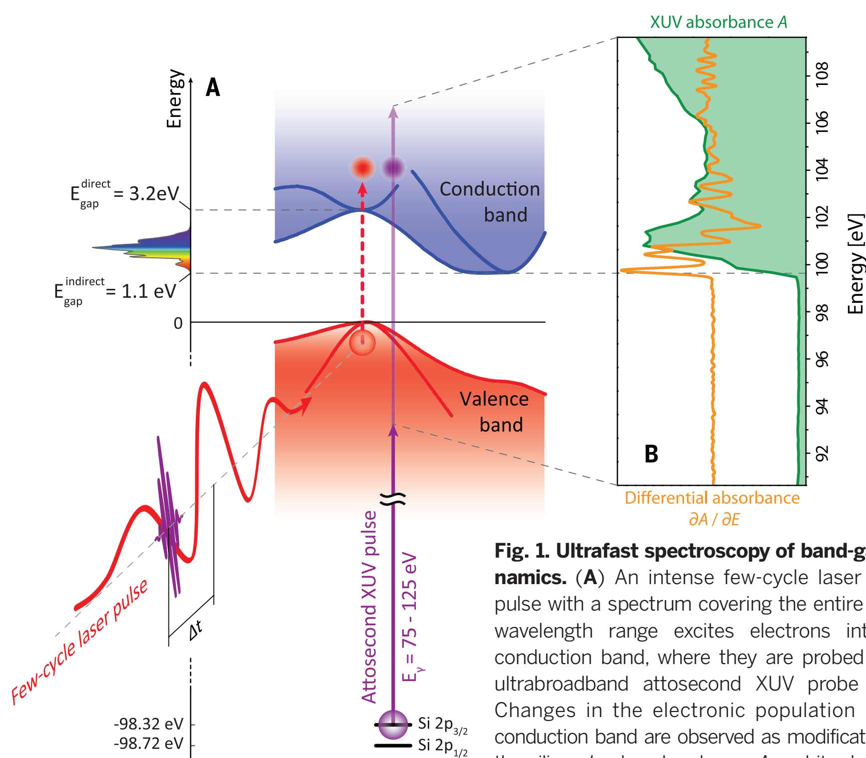

Fig. 1. Ultrafast spectroscopy of band-gap dynamics. (**A**) An intense few-cycle laser pump pulse with a spectrum covering the entire visible wavelength range excites electrons into the conduction band, where they are probed by an ultrabroadband attosecond XUV probe pulse. Changes in the electronic population of the conduction band are observed as modifications of the silicon *L*-edge absorbance *A* and its derivative ∂*A*/∂*E* (**B**). By varying the time delay Δ*t* between the two pulses, dynamic changes to the *L*-edge spectrum can be tracked and translated into the evolution of the conduction band population.

Downloaded from www.sciencemag.org on December 11, 2014

materials (SM), section S2], and span a spectrum of extreme ultraviolet (XUV) photon energies covering 80 to 125 eV. This spectral range probes the density of empty electronic states in a time-resolved variant of x-ray absorption near-edge structure spectroscopy (XANES) (16). Figure 1B shows the recorded silicon L-edge absorbance A of a 250-nm-thick single crystalline free-standing silicon membrane (17) in the <100> orientation, as well as the derivative of the static absorbance $\partial A/\partial E$ as a function of the XUV photon energy E_{XUV} computed from the raw data, which facilitates assessment of excitation-induced broadening and shifts of the CB features. The above-edge structure of $A(E_{XUV})$ recorded by attosecond pulses is a sensitive probe of an extended region of the CB density of states, which is validated by calculated core-level transition spectra (see SM, section S9). Whereas the initial state of the electron undergoing the XUV probe transition is a $2p$ core orbital, the final state of both the XUV probe and the NIR pump excitation lies within the CB manifold. Electron interactions in the CB that alter the XUV transition thus render attosecond XUV absorption sensitive to the evolution of the pump-laser–induced CB population.

The silicon sample is irradiated by ultrashort NIR laser pulses comprising only a few oscillations of the electric field and attaining intensities between 10^{10} and 10^{14} W/cm^2 at the focus, corresponding to a vacuum peak amplitude E_0 of the electric field between 0.02 and 2 V/Å. The laser-induced transfer of electrons to the CB results in a wealth of modifications to the XUV transition. Figure 2A displays the derivative of the L-edge absorbance spectrum, $\partial A/\partial E$, as a function of time delay Δt between the NIR-pump and the XUV-probe pulses. Excitation of silicon by a few-cycle NIR laser pulse, with an intensity inside the sample of $I_{int} = 1.9 \times 10^{12}$ W/cm^2 (see SM, section S5 for the relation between I_{int} and the vacuum intensity I_{vac}), results in a global broadening of the substructures. Most important, as seen in Fig. 2B, the spectrum recorded with carrier-envelope-phase (CEP) stabilized NIR pump pulses evolves with a step-like behavior synchronized with the half-cycle period of the pump electric field oscillations, indicative of subfemtosecond population transfer and carrier-carrier scattering time scales. Further, an effective reduction of the measured band gap (band-gap narrowing) after the excitation is observed (Fig. 2C, blue line), and during the excitation pulse, a transient field–induced blue shift of the L-edge onset is recorded (Fig. 2C, red line). Finally, Fig. 2D shows a clear biexponential decay of the signal recorded over an extended delay range with time constants of 5 fs and 60 fs, respectively, indicating the transition between purely electronic initial response after the laser pulse and convoluted electronic-lattice dynamics at longer time scales.

The L-edge substructures exhibit a global broadening, as shown in Fig. 2A. Electron-electron interactions in the CB cause a modification of the dipolar oscillations associated with optical transitions in the time domain and thus have been previously indicated as the origin of spectral broadening in static studies (18). Similarly, the interaction of XUV probe-promoted electrons with the high density of light-field–injected carriers leads to rapid damping or dephasing of the oscillating XUV transition dipole observed as frequency domain broadening of the L-edge features during and after excitation.

Figure 2B shows the appearance of sharp steps in the L-edge transmittance evaluated at 100.35 eV, in synchrony with the CEP stabilized pump laser electric field oscillations. As the delay between the attosecond probe pulse and the few-cycle pump pulse is scanned, the steps on the rising edge of the time trace are formed when each half-cycle of the electric field of the pump pulse excites electrons from the VB to the CB, leading to synchronized observable changes to the L-edge transition. The rise time of each step

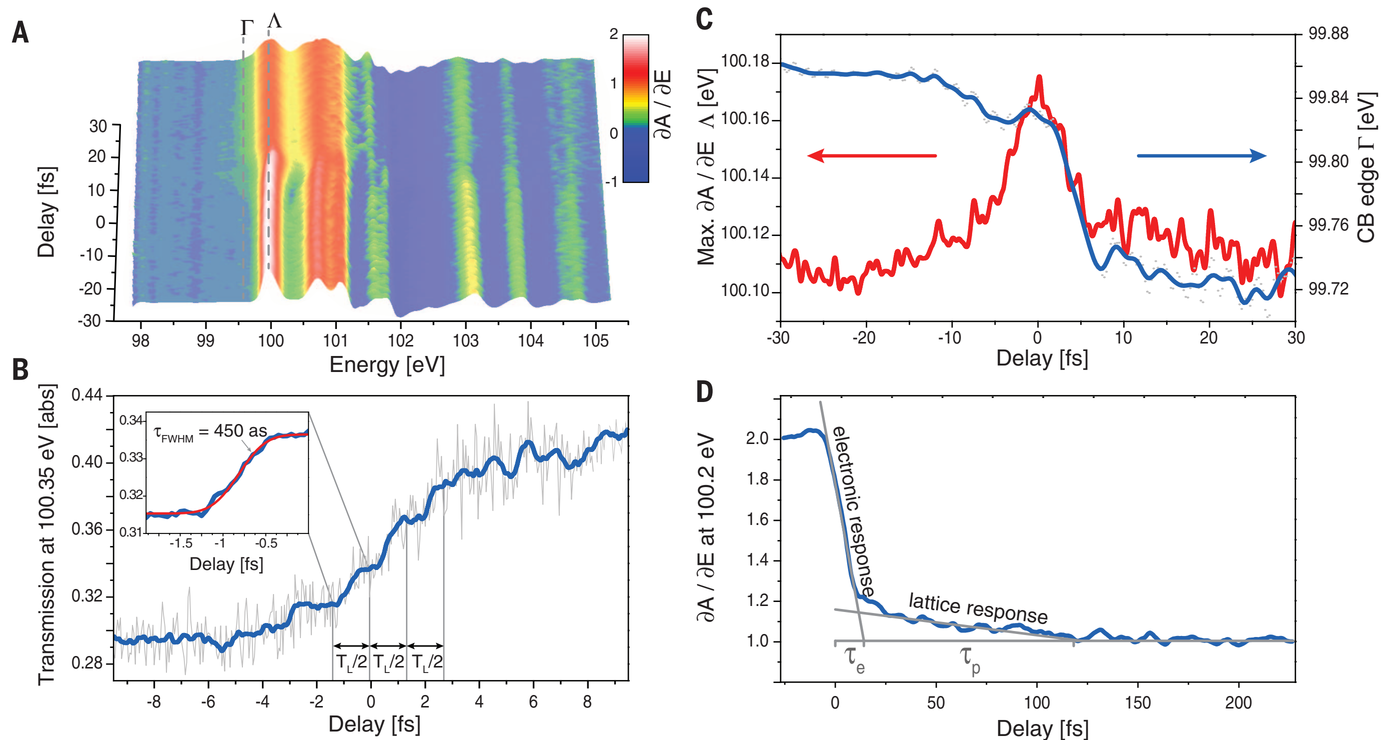

Fig. 2. Attosecond transient absorption spectroscopy of silicon. (**A**) The injection of electrons into conduction band states of silicon by a few-cycle near-infrared laser pump-pulse modifies the derivative of the XUV-absorbance $\partial A/\partial E$ plotted as a function of probe-photon energy E_{XUV} and time delay Δt between pump and probe pulse. The color scale represents the value of $\partial A/\partial E$. (**B**) A close-up of the temporal evolution of the XUV-transmission T (= 10^{-A}) at 100.35 eV reveals the increase of the signal amplitude in sharp steps synchronized with the laser electric field oscillations (also see Fig. 3B). The inset shows a fit to evaluate the step rise time. The blue line is a rolling average of the raw signal depicted in gray. (**C**) The position in energy of the first peak of the derivative [marked Λ in (A)] is plotted (red), along with the energy of the L-edge onset (marked Γ) evaluated at $\partial A/\partial E = 0.2$ (blue). (**D**) tracks the amplitude of $\partial A/\partial E$ at 100.2 eV, the position of the maximum $\partial A/\partial E$ before excitation. The straight lines indicate the different time scales over which electronic (τ_e) and nuclear (τ_p) dynamics occur.

in the subcycle evolution allows an estimate of the response time of the electronic ensemble by fitting an error function with a best-fit full-width half-maximum of ~450 attoseconds (see Fig. 2B inset and SM, section S4), providing an upper limit for the carrier-carrier scattering time in heavily photodoped silicon. An assumed longer response time would obscure the steplike signal evolution, as detailed in the SM, section S4. The findings substantiate the reported sub-1-fs (*19*) estimate for CB electron scattering times in dense electron-hole plasmas.

To develop an understanding of the time evolution of the physical processes dictating the interaction of the few-cycle laser pulses with silicon, we performed ab initio TD-DFT calculations (*20*) within the adiabatic local density approximation (*21*). By predicting the excitation process from first principles without tunable parameters, the simulations quantify the increase in the number of excited electrons with time and their distribution in real and momentum space after the excitation. For intensities up to one order of magnitude of the limit for dielectric breakdown of the sample, the TD-DFT treatment of the excitation dynamics predicts an increase in the number of excited electron hole pairs (Fig. 3A) following the oscillations of the laser electric field, analogous to the stepwise signal evolution shown in Fig. 2B. As input for the simulations, we employed the temporal electric field evolution of the few-cycle NIR driver pulses (Fig. 3B), as recorded by means of attosecond streaking (*22*) of photoelectrons released from neon (see SM, section S2).

When the NIR excitation field is acting on the system, it mixes the CB and VB states and causes tunneling of electrons across the direct band gap. Remarkably, the theory predicts a deviation of the excitation energy per electron-hole pair (Fig. 3C) and of the number of excited electrons per atom (Fig. 3D), from the multiphoton to the field-induced tunneling regime. Field-induced tunneling dominates for laser intensities that correspond to a value of the Keldysh adiabaticity parameter $\gamma < 1$, defined as $\gamma = \frac{\omega}{eE_0}\sqrt{m^*\Delta_g}$, where Δ_g, ω, and m^* are the band gap of the material, the laser frequency, and the reduced mass of the electron hole pair (here, $0.25\ m_e$), respectively (*23*). At the intensity of 1.9×10^{12} W/cm^2 used in the experiment, $\gamma \sim 0.5$, which suggests that the excitation mechanism is within the tunneling regime.

The insets in Fig. 3 display a spatial representation of the ultrafast band-gap excitation derived from the TD-DFT calculation. Modifications of the spatial electronic density distribution along a cut through the eight-atom unit cell in the [011] × [100] plane are shown relative to the ground state. During the laser pulse (panels t_1 and t_2), field-driven dipolar oscillations along the silicon-silicon bond dominate. After the laser electric field passes (panel t_3), some electronic density along the interatomic bonds is depleted, and the density is relocated to the interstitial regions that represent the mobile antibonding conduction band states of the crystal.

The validity of the predicted CB electron energy distribution and the identification of field-induced tunneling as the main excitation mechanism are corroborated by the experimental observations at a laser intensity of $I_{\mathrm{int}} = 1.9 \times 10^{12}$ W/cm^2. The calculations indicate that the occupation number profile of hole states exhibits a narrow distribution below the VB (mean value 0.5 eV below VB maximum) compared with the electrons in the CB, where the mean value of the distribution is at 2.1 eV above the CB minimum. Carrier-induced changes to the XUV absorbance are detected experimentally up to 6 eV above the band gap (see Fig. 2A and SM, section S6), beyond which the signal-to-noise ratio limits further measurements.

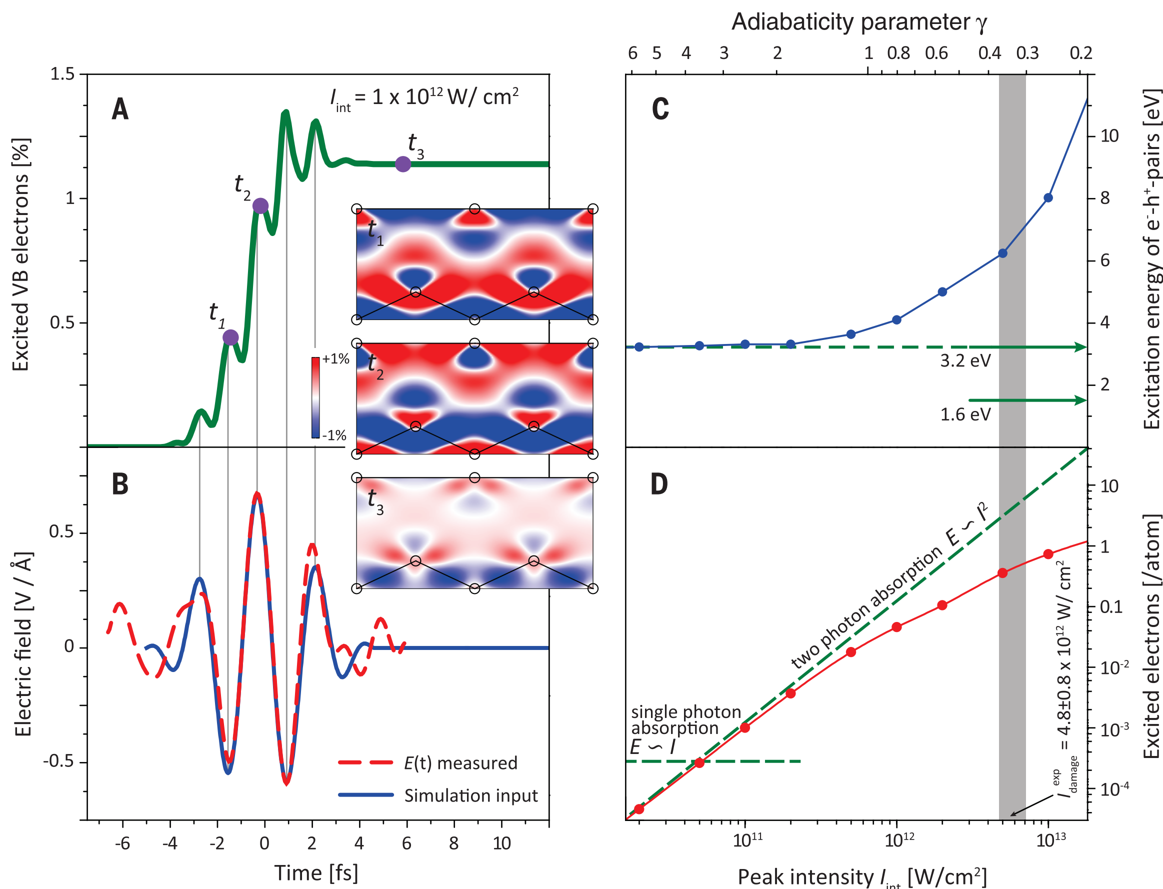

Fig. 3. Theoretical simulations of subfemtosecond population transfer in silicon. (**A**) Number of electrons excited into the conduction band by a 4.8-fs laser pulse of peak intensity inside silicon of 1×10^{12} W/cm^2, as predicted by TD-DFT calculations. The extent of population transfer is quantified as a percentage of the initially available valence band electrons. As input for the calculations, a theoretical laser waveform [blue line in (**B**)] was used that was fitted to the laser electric field evolution extracted from an attosecond streaking measurement [red dashed line in (B)]. Gray lines between (A) and (B) identify the laser field extrema and the corresponding oscillations in (A). The insets show the calculated electronic density distribution during (t_1 and t_2) and after (t_3) the passage of the excitation pulse along the crystal plane defined by the [011] and [100] axes. The red and blue colors represent enhancement and depletion of electronic density, respectively, relative to the ground-state distribution. The calculated (**C**) mean excitation energy per electron-hole pair and (**D**) number of excited electrons plotted as a function of laser peak intensity inside the material deviate from the expectations for two-photon absorption behavior for values of the adiabaticity parameter <1, indicating transition into the light-field–induced tunneling regime.

These observations are irreconcilable with a multiphoton excitation mechanism, which would promote electrons to states concentrated at the band edge. In contrast, the electrons have an increasing amount of excess energy above the band gap as the laser intensity is increased, in agreement with experimental observations of an intensity-dependent extent of above-gap changes in the XUV transitions (see SM, section S6). The width of the above-gap excitation distribution is in accord with TD-DFT calculations, which predict that the number of excitation events compared with the expectation based on 2-photon absorption is truncated (Fig. 3, C and D). Concomitantly, the theory allows us to explore the intensity dependence of the population transfer and suggests that below the experimentally observed threshold for permanent sample damage of I_{int} = 4.8×10^{12} W/cm^2 (I_{vac} = 2.7×10^{13} W/cm^2) (see SM, section S5), more than 10% population transfer can be established during the few-cycle laser pulse (Fig. 3D).

After the NIR excitation, the measurements reveal a lasting shift of the *L*-edge absorption onset (i.e., the CB minimum) to a 121 meV lower value, as evaluated at $\partial A/\partial E = 0.2$ of the *L*-edge spectral derivative (blue line in Fig. 2C). We performed core-level absorption calculations (*24*) with the electronic excitation density distribution obtained from the TD-DFT treatment (details in the SM, section S7) to obtain transient core-level spectra and relate the observed shifts to the number of excited carriers. The calculations reveal that Pauli state–blocking under these conditions has an insignificant influence on the XUV transition, owing to the dilute above-gap state occupation resulting from the tunneling process. The calculations furthermore estimate a core-level shift ΔE_{CL} following the band-gap excitation of 43 meV toward lower binding energy (see SM, section S9), rooted in the additional screening response of the excited carriers. This prediction on the single-particle level of theory disregards electron-electron interactions in the CB and reflects only 30% of the experimentally observed lasting red shift of the CB onset. In contrast, many-body core absorption theory, so far restricted to an equilibrated electronic CB population, confirms that the observed effective red shift of the CB onset (78 meV) is due to electron-electron interactions causing band-gap narrowing and increased above-gap electron scattering rates (see SM, section S9).

Valence and conduction bands are reported to shift by identical amounts in the presence of electron-hole pairs (*18*), and comparison with band-gap displacements observed as a function of doping concentration (*12*) suggests that ~10^{21}/cm^3 electron-hole pairs are created by the pump pulse. In striking agreement with this estimate, the ab initio TD-DFT calculations predict that after a 4.8-fs NIR pulse with an intensity of $I_{int} = 1 \times 10^{12}$ W/cm^2, 1.2% of all the valence electrons are excited into the CB, resulting in a carrier density of ~2.3×10^{21} cm^{-3} and a corresponding increase in conductivity of seven orders of magnitude (*25*) (see SM, section S12). The excitation-induced broadening of the spectral features (Fig. 2A) is observed for at least 200 fs, suggesting the persistence of the population transfer beyond the time scale sampled in these experiments.

Transiently, the experimental spectrum manifests a field-induced blue shift of the *L*-edge transition during the pump pulse (Fig. 2C, red line). In the presence of the excitation field, the XUV transition has to bridge the core-level-to-CB energy difference and provide the ponderomotive energy for the electron to oscillate in the field (*26*), analogous to the core-to-continuum transition in atoms dressed by an external field (*27*). The observed transient blue shift of ~80 meV is smaller than the calculated ponderomotive energy of 112 meV for a laser intensity of I_{int} = 1.9×10^{12} W/cm^2, owing to the competing transient red shift of the XUV transition due to the quadratic Stark effect. This acts to lower both the 2*p* core level and the CB minimum, but by different magnitudes due to the higher polarizability of the delocalized CB states. Core-level absorption calculations indeed predict a counteracting red shift of the *L*-edge transition under the influence of the laser field but do not yield quantitative agreement with the experiment. This discrepancy likely reflects disregard of the dynamical polarizability of the partially populated CB manifold, a subject for future theoretical developments. Both effects appear fully reversible and disappear after the passage of the few-cycle pump pulse.

On the time scale characteristic of lattice dynamics, tens of fs and longer, the experiments reveal participation of lattice modifications. Figure 2D shows the amplitude of $\partial A/\partial E$ at 100.2 eV, the photon energy corresponding to maximum $\partial A/\partial E$ before excitation. About 80% of the persistent pump-induced changes of the XUV absorbance are established immediately during the laser electric field and can be attributed to the ultrafast electronic response already discussed. When the temporal behavior of the amplitude of the derivative is fit with a biexponential decay (see SM, section S10) with time constants of τ_e and τ_p, the residual ~20% change in the amplitude is governed by a time scale of $\tau_p = 60 \pm 10$ fs, characteristic of the fastest optical phonon, which has a period of 64 fs (*14*, *15*). The TD-DFT calculations establish that this periodic modulation of the interatomic distances is set in motion when electrons tunnel from VB states located in the interatomic bond region to the interstitial CB states (Fig. 3, insets). As a result, the XUV transition exhibits an inhomogeneous broadening as the transmitted XUV pulse averages over many periods of the phonon motion and the associated interatomic distances. Indeed, the core-level absorption calculations indicate that an additional 20% spectral broadening of the XUV transition beyond the electronic response is expected over one full period of the longitudinal optical (LO) phonon vibration assuming 6-picometer atomic displacement (SM, section S10). In these experiments, we do not expect to observe periodic recurrences of the LO phonon in the time span sampled because of the insensitivity of the transmitted XUV pulse to the phase of the lattice vibration. Furthermore, fully coherent motion sets in only beyond 2 ps (*15*), before which higher harmonics of the vibration interfere and result in aperiodic modulation of the signal. The observation of a temporal hierarchy in the coupled electron-lattice response validates the widely employed phenomenological two-temperature model describing energy relaxation in solids (*28*). There, an impulsive excitation is assumed to primarily raise the electronic temperature followed by a heating of the lattice by the hot electrons. These results also highlight the fact that, due to the mismatch between almost instantaneous electronic and delayed lattice response, ultrashort excitation pulses can cause percent-level carrier excitation quasi-instantaneously without substantial lattice distortion or sample damage.

The presented methodology could generally explore the dynamics of light-induced excitation processes in semiconductors independent of the excitation mechanism. The ability to separate electronic and lattice response to an initial population transfer will permit the investigation of postexcitation carrier interactions and relaxation dynamics.

Through analysis of the experimental *L*-edge spectra at different time delays, in combination with TD-DFT and core-level absorption calculations, these studies reveal the time scale of carrier-carrier interactions and identify their role in the band-gap reduction of semiconductors. The attosecond temporal resolution allows identification of light-field–driven electron tunneling as the main process for band-gap excitation by few-cycle near-infrared laser pulses.

REFERENCES AND NOTES

1. J. Shah, *Ultrafast Spectroscopy of Semiconductors and Semiconductor Nanostructures* (Springer, Berlin, New York, 1996).
2. F. Krausz, M. I. Stockman, *Nat. Photonics* **8**, 205–213 (2014).
3. W. F. Koehl, B. B. Buckley, F. J. Heremans, G. Calusine, D. D. Awschalom, *Nature* **479**, 84–87 (2011).
4. P. T. Greenland *et al.*, *Nature* **465**, 1057–1061 (2010).
5. M. Lenzner *et al.*, *Phys. Rev. Lett.* **80**, 4076–4079 (1998).
6. D. Du, X. Liu, G. Korn, J. Squier, G. Mourou, *Appl. Phys. Lett.* **64**, 3071 (1994).
7. M. Gertsvolf, M. Spanner, D. M. Rayner, P. B. Corkum, *J. Phys. At. Mol. Opt. Phys.* **43**, 131002 (2010).
8. P. C. Becker *et al.*, *Phys. Rev. Lett.* **61**, 1647–1649 (1988).
9. W. Kuehn *et al.*, *Phys. Rev. Lett.* **104**, 146602 (2010).
10. J. Noffsinger, E. Kioupakis, C. G. Van de Walle, S. G. Louie, M. L. Cohen, *Phys. Rev. Lett.* **108**, 167402 (2012).
11. M. Beye *et al.*, *New J. Phys.* **12**, 043011 (2010).
12. R. J. Van Overstraeten, R. P. Mertens, *Solid-State Electron.* **30**, 1077–1087 (1987).
13. M. Schultze *et al.*, *Nature* **493**, 75–78 (2013).
14. Y. Shinohara *et al.*, *Phys. Rev. B* **82**, 155110 (2010).
15. M. Hase, M. Katsuragawa, A. M. Constantinescu, H. Petek, *Nat. Photonics* **6**, 243–247 (2012).
16. D. C. Koningsberger, R. Prins, Eds., *X-ray Absorption: Principles, Applications, Techniques of EXAFS, SEXAFS, and XANES* (Wiley-Interscience, New York, ed. 1, 1988).
17. Silicon crystals 250 nm thick, lightly p-doped (Boron dopant, 1.5×10^{15}/cm^3), have been obtained from Norcada, Inc. For the subcycle-resolved measurement, the samples have been thinned in a plasma etching protocol to a final layer thickness of 140 nm.
18. L. Viña, M. Cardona, *Phys. Rev. B* **29**, 6739–6751 (1984).

19. D. Hulin, A. Mourchid, R. Vanderhaghen, P. M. Fauchet, in *Ultrafast Phenomena VII SE - 85*, Springer Series in Chemical Physics. C. Harris, E. Ippen, G. Mourou, A. Zewail, Eds. (Springer, Berlin Heidelberg, 1990), vol. 53, pp. 282–284.
20. K. Yabana, T. Sugiyama, Y. Shinohara, T. Otobe, G. F. Bertsch, *Phys. Rev. B* **85**, 045134 (2012).
21. J. P. Perdew, A. Zunger, *Phys. Rev. B* **23**, 5048–5079 (1981).
22. R. Kienberger *et al.*, *Nature* **427**, 817–821 (2004).
23. L. V. Keldysh, *Sov. Phys. J. Exp. Theor. Phys.* **20**, 1307–1314 (1965).
24. D. Prendergast, G. Galli, *Phys. Rev. Lett.* **96**, 215502 (2006).
25. W. R. Thurber, R. L. Mattis, Y. M. Liu, J. J. Filliben, *J. Electrochem. Soc.* **127**, 2291–2294 (1980).
26. A. Srivastava, R. Srivastava, J. Wang, J. Kono, *Phys. Rev. Lett.* **93**, 157401 (2004).
27. P. Radcliffe *et al.*, *New J. Phys.* **14**, 043008 (2012).
28. P. B. Allen, *Phys. Rev. Lett.* **59**, 1460–1463 (1987).

ACKNOWLEDGMENTS

We acknowledge fruitful discussions with P. Feulner and help with sample preparation from R. Rivers. The experimental work is supported by the Office of Assistant Secretary of Defense for Research and Engineering through a National Security Science and Engineering Faculty Fellowship (NSSEFF), with additional funding from the Defense Advanced Research Projects Agency PULSE program through grant W31P4Q-13-1-0017. The W. M. Keck Foundation and the Department of Energy under contract DE-AC03-76SF00098 are acknowledged for additional experimental equipment. S.R.L. and D.M.N. acknowledge Multidisciplinary University Research Initiatives from the Army Research Office (WN911NF-14-1-0383) and the Air Force Office of Scientific Research. S.A.S and K.Y. performed computations at the Institute of Solid State Physics, University of Tokyo under Japan Society for the Promotion of Science KAKENHI grants 23340113 and 25104702. M.S. was supported by a Marie Curie International Outgoing Fellowship (FP7-PEOPLE-2011-IOF). C.D.P. and D.P. performed work at the Molecular Foundry, supported by the Office of Science, Office of Basic Energy Sciences, of the U.S. Department of Energy under contract DE-AC02-05CH11231, with computing resources at Lawrence Berkeley National Laboratory and the National Energy Research Scientific Computing Center (NERSC).

SUPPLEMENTARY MATERIALS

www.sciencemag.org/content/346/6215/1348/suppl/DC1
Materials and Methods
Figs. S1 to S16
References (*29*–*59*)

22 August 2014; accepted 10 November 2014
10.1126/science.1260311

NANOLITHOGRAPHY

Large-scale nanoshaping of ultrasmooth 3D crystalline metallic structures

Huang Gao,[1,3*] Yaowu Hu,[1,3*] Yi Xuan,[2,3*] Ji Li,[1,3] Yingling Yang,[1,3] Ramses V. Martinez,[4,5] Chunyu Li,[3,6] Jian Luo,[7] Minghao Qi,[2,3] Gary J. Cheng[1,3,8†]

We report a low-cost, high-throughput benchtop method that enables thin layers of metal to be shaped with nanoscale precision by generating ultrahigh-strain-rate deformations. Laser shock imprinting can create three-dimensional crystalline metallic structures as small as 10 nanometers with ultrasmooth surfaces at ambient conditions. This technique enables the successful fabrications of large-area, uniform nanopatterns with aspect ratios as high as 5 for plasmonic and sensing applications, as well as mechanically strengthened nanostructures and metal-graphene hybrid nanodevices.

Nanoscale metallic structures and their possible uses are under investigation in a variety of fields such as plasmonics (*1*), electronics (*2*), and biosciences (*3*). However, the large-scale manufacture of such structures with high fidelity and quality [e.g., ultrasmooth surfaces, sharp corners, three-dimensional (3D) shapes, and high crystallinity] represents a substantial challenge. Although nanoimprint lithography is a useful method of fabricating nanometer-scale patterns on polymers (*4*, *5*) and has been adapted to metallic glasses (*6*), direct nanoimprinting of crystalline metals is still generally infeasible because of the limitations on formability arising from (i) fluctuations of plasticity at the nanoscale caused by localized dislocation bursts (*7*, *8*), (ii) size effects in plasticity (*9*, *10*), and (iii) grain size effects, which generally limit the feature size to be larger than the grains (*11*, *12*). These limitations can be circumvented by using nanocrystalline or amorphous metals (*6*), heating the sample close to melting temperature (*13*), or using a superhard mold (*14*). But these methods either place limits on the materials that can be used, or operate at high temperatures with serious drawbacks [e.g., the heating and solidification cycle in hot embossing (*14*) or melting (*15*) leads to high surface roughness, especially in sub–100-nm metallic structures]. Moreover, the low crystallinity in metallic glasses limits their functionality because of electric and magnetic losses (*16*). Similarly, fabrication of metal nanopatterns by direct nanoimprinting of nanoparticles (*17*) incurs size effects of the particles during their deposition into the nanomolds and is therefore not a good choice for ultrafine patterns. Currently, fabrication of metallic nanopatterns relies on time-consuming, multistep approaches consisting of electron beam lithography (*18*, *19*) or template stripping (*20*, *21*). However, high resolution, high crystallinity, and low sidewall roughness cannot be achieved simultaneously, even with state-of-the-art equipment.

Figure 1A summarizes the most common direct shaping processes, materials, ranges of their respective processing strain rates, and processing temperatures. A key barrier that impedes the fabrication of smooth ultrafine crystalline metallic 3D nanostructures is the high strain rate required to activate superplasticity in metals, due to the need of ultrafine grain/particle sizes to generate superplastic flows (*22*, *23*). Unfortunately, the existing imprinting methods cannot provide sufficient high strain rates to generate 3D metallic crystalline nanostructures.

We demonstrate "laser shock imprinting" (LSI), a cost-effective direct nanoshaping method for high-throughput fabrication of smooth 3D crystalline nanostructures at ambient conditions. LSI uses a laser shock to compress metallic sheets into a silicon nanomold with a variety of shapes. We have used the nanomolds for over a hundred times with no damage or degradation in performance (fig. S1). This technique enables large-scale direct fabrication of smooth ultrafine metallic nanopatterns as small as 10 nm for mass production (fig. S2). LSI uses ultrahigh–strain rate deformation at room temperature to overcome the limitations in nanoscale formability of coarse-grained metals. Additionally, LSI can be applied to a broad range of metals, including metals as hard as Ti (fig. S3).

Figure 1B schematically illustrates the LSI process. We used a Nd:YAG laser pulse (0.3 to 1.4 GW/cm^2, wavelength 1064 nm, pulse duration ~5 ns) to irradiate an ablation coating layer (10 μm graphite) in direct contact with the sample. The sublimation of the ablation layer by the laser pulse generates a shock wave that, constrained by the confinement layer (glass or water), propagates through the metallic sheet and plastically deform it conformably on the underlying silicon mold with nanoscale resolution. According to Fabbro's model (*24*), the peak pressure of the shock wave generated by the laser pulse reaches 0.85 to 1.83 GPa, enabling the generation of strain rates on the order of 10^6 to 10^7 s^{-1} during the laser shock, depending on the applied laser intensity and pulse duration.

We fabricated silicon nanomolds by e-beam lithography (EBL) and reactive ion etching (RIE) or wet etching. Atomic layer deposition (ALD) was used to deposit an ultrathin Al_2O_3 layer (5 to

[1]School of Industrial Engineering, Purdue University, West Lafayette, IN 47907, USA [2]School of Electrical and Computer Engineering, Purdue University, West Lafayette, IN 47907, USA [3]Birck Nanotechnology Center, Purdue University, West Lafayette, IN 47907, USA [4]Department of Chemistry and Chemical Biology, Harvard University, Cambridge, MA 02138, USA [5]Madrid Institute for Advanced Studies, IMDEA Nanoscience, Ciudad Universitaria de Cantoblanco, 28049 Madrid, Spain. [6]School of Materials Engineering, Purdue University, West Lafayette, IN 47907, USA. [7]Department of NanoEngineering, University of California, San Diego, La Jolla, CA 92093, USA. [8]School of Mechanical Engineering, Purdue University, West Lafayette, IN 47907, USA.
*These authors contributed equally to this work. †Corresponding author. E-mail: gjcheng@purdue.edu

EXTENDED PDF SPONSORED
BY BIO-TECHNE.COM

Attosecond band-gap dynamics in silicon

Martin Schultze *et al.*

Science **346**, 1348 (2014);
DOI: 10.1126/science.1260311

This copy is for your personal, non-commercial use only.

If you wish to distribute this article to others, you can order high-quality copies for your colleagues, clients, or customers by clicking here.

Permission to republish or repurpose articles or portions of articles can be obtained by following the guidelines here.

The following resources related to this article are available online at www.sciencemag.org (this information is current as of December 11, 2014):

Updated information and services, including high-resolution figures, can be found in the online version of this article at:
http://www.sciencemag.org/content/346/6215/1348.full.html

Supporting Online Material can be found at:
http://www.sciencemag.org/content/suppl/2014/12/11/346.6215.1348.DC1.html

A list of selected additional articles on the Science Web sites **related to this article** can be found at:
http://www.sciencemag.org/content/346/6215/1348.full.html#related

This article **cites 53 articles**, 2 of which can be accessed free:
http://www.sciencemag.org/content/346/6215/1348.full.html#ref-list-1

This article has been **cited by** 1 articles hosted by HighWire Press; see:
http://www.sciencemag.org/content/346/6215/1348.full.html#related-urls

This article appears in the following **subject collections:**
Physics
http://www.sciencemag.org/cgi/collection/physics

Downloaded from www.sciencemag.org on December 11, 2014

Science (print ISSN 0036-8075; online ISSN 1095-9203) is published weekly, except the last week in December, by the American Association for the Advancement of Science, 1200 New York Avenue NW, Washington, DC 20005. Copyright 2014 by the American Association for the Advancement of Science; all rights reserved. The title *Science* is a registered trademark of AAAS.